Dalton Transactions

Accepted Manuscript

ROYAL SOCIETY OF CHEMISTRY

www.rsc.org/dalton

Dalton Transactions

ARTICLE TYPE

Guanidine sulfate-assisted synthesis of hexagonal WO_3 nanoparticles with enhanced adsorption properties

Wanjun Mu, Mei Li, Xingliang Li, Zongping Ma, Rui Zhang, Qianhong Yu, Kai Lv, Xiang Xie, Jiaheng He, Hongyuan Wei*, Yuan Jian

Received (in XXX, XXX) Xth XXXXXXXXX 20XX, Accepted Xth XXXXXXXXX 20XX
DOI: 10.1039/b000000x

Large surface area hexagonal phase WO_3 (h-WO_3) nanowires were synthesized by a hydrothermal route with the assistance of $C_2H_{12}N_6O_4S$. They were characterized by XRD, SEM, TEM, BET, FT-IR and XPS. It is shown that not only $C_2H_{12}N_6O_4S$ acts as a stabilizer to facilitate the generation of a metastable hexagonal phase, but also function as a structure directing agent to assist the construction of nanowires. The obtained h-WO_3 possesses a large specific surface area and numerous adsorption functional groups such as −OH groups. These characteristics result in excellent adsorption performance for the removal of strontium from acidic aqueous solutions. A maximum adsorption capacity of 52.93 mg g^{-1} was achieved on the h-WO_3 prepared in the presence of $C_2H_{12}N_6O_4S$. This value is almost two times higher than that of bare h-WO_3 (no $C_2H_{12}N_6O_4S$). The effects of pH, contact time, initial Sr^{2+} concentration and ion strength on Sr^{2+} removal from the solution by h-WO_3 were systematically investigated. The adsorption mechanism involving the combination of electrostatic attraction and ion exchange for the adsorption of Sr^{2+} is proposed. Based on our results, h-WO_3 with high adsorption capacity and good surface characteristics exhibited great potential for the removal of Sr^{2+} from radioactive wastewater.

1 Introduction

Increasing use of nuclear power plants and nuclear laboratories results in radioactive waste solutions being released into the environment. The main radionuclides in these solutions include fission products such as ^{90}Sr and ^{137}Cs. These species cause serious environmental problems worldwide. [1-2] The selective separation of radioactive nuclides from nuclear waste solutions would be a highly effective method to minimize nuclear waste volumes for final disposal.[3] Because of their radiation stability and high selectivity, inorganic ion exchange materials lend themselves to the treatment of nuclear waste solutions. Several inorganic ion exchange materials such as zeolites,[4] metal sulfides,[5] silicotitanates[6] and clay minerals[7] are typically used at nuclear sites for the separation of ^{90}Sr and ^{137}Cs from the nuclear waste mix. However, the application of these materials is limited by their relatively narrow operating pH range and slow ion exchange kinetics. For example, hydrous antimony pentoxide (antimonic acid) $Sb_2O_5{\cdot}4H_2O$ is an ion exchanger that features a pyrochlore structure and its ion exchange properties have been extensively studied.[8-10] However, it shows poor performance toward the selective adsorption of Sr^{2+} under acidic solutions. Therefore, an ideal ion exchanger possesses good acid-resistance properties and is particularly selective toward important waste radionuclides such as ^{90}Sr when present in a mix under harsh conditions.

Hexagonal tungstate oxide (h-WO_3) has received much attention because of its tunnel structure in which WO_6 octahedra share their corners to form hexagonal tunnels along the c-axis.[11-12] Guest ions such as Na^+, NH_4^+ reside in the "hexagonal window" tunnels between the layers and can be exchanged by ions such as K^+, Cs^+. Moreover, it has been reported that *h*-WO_3 or **Nb-doped *h*-WO_3** is an adsorbent that removes radionuclides (including Sr^{2+}) from acidic solutions.**[13-15]** However, it has a low adsorption capacity toward Sr^{2+}. Many studies have reported that nanoadsorbents with large specific surface areas and rich surface functional groups are excellent at the in-depth removal of metal ions from wastewater.[16] A variety of nanostructured WO_3 materials have been prepared, including nanofilms,[17] nanosheets,[18] nanowires [19] and nanotubes.[20] Induced anisotropic growth using specific capping agents is a strategy for the preparation of complex nanomaterials.[21] It is reported that sulfates are considered capping reagents such as Li_2SO_4,[22] Na_2SO_4,[23] $NaHSO_4$[24] and $(NH_4)_2SO_4$[25] are used in the preparation of WO_3 processes, because SO_4^{2-} ions play many important roles in directing the morphology of the final product. Despite some outstanding results having been achieved the small surface areas obtained restrict their adsorption applications. Nevertheless, as-synthesized WO_3 adsorbents have few surface functional groups apart from W=O groups resulting in a remarkable reduction in their adsorption activities. Therefore, it is becoming important to fabricate nanoadsorbents with larger surface areas and abundant functional groups (such as -OH) that cover their surfaces.

Guanidine sulfate ($C_2H_{12}N_6O_4S$, Fig.1) is a compound that releases CO_2 gas, NH_4^+ ions and SO_4^{2-} ions in hydrothermal reaction processes.[26-27] Theoretically, the gas produced can increase the surface area of nanomaterials during their growth processes and SO_4^{2-} ions can influence the crystal phase and morphology of h-WO_3. **Additionally, $C_2H_{12}N_6O_4S$ that dissolves in the aqueous solution forms a large number of**

NH_4^+ ions in aqueous solution. However, this process only a hypothesis since no reports exist where $C_2H_{12}N_6O_4S$ has been used as a capping agent during the synthesis of h-WO_3 for use as an adsorbent.

In this work, nanostructured h-WO_3 was successfully synthesized with the addition of $C_2H_{12}N_6O_4S$ as a structure directing agent. Characterization shows that the prepared sample exhibits relatively high surface areas and abundant hydroxyl groups on the surface. They also provide a large number of adsorbent sites and efficient chelating sites to coordinate with Sr^{2+} ions. The adsorption experiment indicated that the h-WO_3 prepared in presence of $C_2H_{12}N_6O_4S$ showed good performance in aqueous solution.

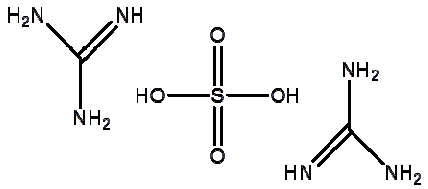

Fig.1 Schematic illustration for the formula of $C_2H_{12}N_6O_4S$

2 Experimental

2.1 Synthesis and characterization

All chemical used were purchased without further deal with unless otherwise specified.

To synthesize 1D WO_3, 2 g $Na_2WO_4{\cdot}2H_2O$ was dissolved in 45 mL deionized water under stirring at room temperature and 5 ml of 3 mol L^{-1} HCl solution was added dropwise into the above solution under continuous stirring. Then **$C_2H_{12}N_6O_4S$** was added in this suspension, followed by transferring into a Teflon-lined autoclave, in which the solution was allowed to remain at 170 °C for 48 h. After that, the autoclave cooled down naturally. The finally products were collected by glassware, then washed with deionized water and ethanol three times, and then dried in air at 80°C.

2.2 Characterization

The crystalline structure of as-prepared samples were characterized using an X-ray diffraction (PXRD, X'Pert PRO, PANalytical, Almelo, Netherlands) with Cu-Ka radiation (λ=0.15406 nm at 40 kv and 45 mA). The sizes and shapes of the nanostructures were observed on a field emission scanning electron microscope (FE-SEM Philips XL30 FEG, Eindhoven, Netherlands) and transmission electron microscopy (TEM， JEM200CX, 120 kV). The composition and chemical state of X-Ray photoelectron spectroscopy (XPS) was performed on a RBD upgraded PHI-5000C ESCA system (Perkin-Elmer) using Mg-monochromatic X-ray at a power of 25 W with an X-ray-beam diameter of 10 mm, and a pass energy of 29.35 eV. The binding energy was calibrated by the C1s hydrocarbon peak at 284.8 eV. Nitrogen adsorption and desorption isotherms were measured at 77 K with a Beckman Coulter SA 3100 surface area analyzer. To determine the surface area, the Brunauer–Emmett–Teller (BET) method was used. Zeta Meter (ZetaPALS, BLK, USA) was applied to measure the zata potential of undoped and doped antimony oxide. Fourier transform infrared (FT-IR) spectra of the samples were obtained on a Perkin-Elmer1730 infrared spectrometer in the range of 400-4000cm^{-1}.

2.3 Adsorption capability

Studies on the Sr^{2+} sorption behavior were performed on *h*-WO_3 sample prepared with addition of $C_2H_{12}N_6O_4S$ in batch experiments using 200 mL volume flask. Aqueous solutions of non-radioactive $Sr(NO_3)_2$ were used instead of radioactive isotopes to avoid radiation damage. Solution pH was adjusted and measured on a digital pH-meter (PHS-4CT, China), Using HNO_3 and NaOH solution. To study the adsorption ability of *h*-WO_3 samples in acidic solutions, the pH of the initial solution did not exceed 8. Adsorbent (0.2 g) was added to $Sr(NO_3)_2$ solution (50 mL) at different acidities (pH = 1-7). The effect of $C_2H_{12}N_6O_4S$ content, pH, equilibrium time, temperature and ionic strength were examined. Equilibrium studies were conducted within the Sr^{2+} concentration range of 20-200 mg L^{-1}. Detailed experimental conditions are presented in the related figure captions for clear identification. The solutions were withdrawn from the flasks and separated from the solids by centrifugation, then the initial and the residual concentration of tested ion(s) in supernatants were determined by atomic absorption spectroscopy (AAalyst800, PerkinElmer, USA). The sorption amount q_e (mg g^{-1}) of adsorbed Sr^{2+} ions is calculated as:

$$q_e = \frac{(C_0 - C_e) \times V}{m} \quad (1)$$

where C_0 (mg L^{-1}) is the initial concentration of metal ion, C_e (mg L^{-1}) is the equilibrium concentration, V (L) is the volume of the testing solution and m (g) is sorbent dose.

3. Results and discussion

3.1. Characterization of WO_3 nanostructure

The morphological features of the as-prepared product nanostructures were determined by SEM and TEM. The added $C_2H_{12}N_6O_4S$ had a significant influence on the morphologies of the final products. The pure WO_3 sample (W-1, Fig. 2a) had typical insect-like aggregate features and it contained a large number of tiny nanorods. With the addition of 1.5 g $C_2H_{12}N_6O_4S$ the morphologies of the synthesized WO_3 sample (W-2, Fig. 2b) had a mesh-like appearance and it was composed of aggregated nanorods. However, very minor nanoparticles could still be observed. The mesh-like appearance became more dominant in the sample prepared with 2.5 g $C_2H_{12}N_6O_4S$ (W-3), as shown in Fig. 2c. This material was composed of nanorods and nanowires. Pure and uniform nanowires with lengths around several micrometers and diameters of 30–60 nm were produced with the use of 4 g $C_2H_{12}N_6O_4S$ (W- 4, Fig. 2d). Increasing the amount of $C_2H_{12}N_6O_4S$ led to stacked nanowires with few nanoparticles being generated (Fig. S1). From these results, the content of $C_2H_{12}N_6O_4S$ plays an important role in controlling the morphology of WO_3. To achieve high purity nanowires, a high proportion of $C_2H_{12}N_6O_4S$ is needed. For further insight into the temperature effect, the synthesis of WO_3 with the addition of 4g $C_2H_{12}N_6O_4S$ was also carried out at 200 °C. We found that the morphology did not change appreciably compared with the sample obtained at 170 °C.

Hexagonal phase WO_3 is a metastable phase. Therefore, structure directing agents are essential to stabilize the nuclei and prevent them from significant aggregation.[28] Compared with organic capping reagents that assist with the formation of *h*-WO_3, inorganic capping reagents are facile, controllable and environmental friendly, and are thus more desirable.[29] In this study, $C_2H_{12}N_6O_4S$ was used as the capping agent and its influence on the phases of the hydrothermal products was examined by XRD, as shown in Fig.3. All the diffraction peaks were exclusively indexed to the h-WO_3 crystalline phase with lattice constants of a=7.285 Å and c=3.883 Å (JCPDS # 35-1001). No other impurities are present in the XRD pattern. The strong and sharp diffraction peaks indicate good crystallinity for the as-synthesized products. The XRD peak intensity of the (001) plane is stronger than that of the other planes indicating that the c-axis (001) is the major growth direction. **The Raman spectra of samples was shown in Fig.3b. Well-defined Raman peaks centered at 326cm^{-1},755cm^{-1}, 951cm^{-1} and 1151cm^{-1} can be observed.[30-32] According to the literature, these bonds can be assigned to the fundamental modes of crystalline of h-WO_3. The bonds at 755cm^{-1} are related to O-W-O stretching modes, while the bonds at 326cm^{-1} can be attributed to W-O-W bending mode of the bridging oxygen. The peak at 955cm^{-1} is attributed to the a stretching mode of the terminal W^{+6}=O.**

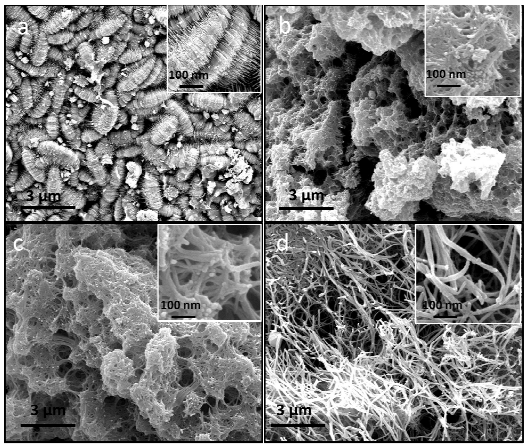

Fig.2 SEM images of the samples obtained by hydrothermal treatment at 170 °C for 24 h after adding: 0 g (a), 1.5 g (b), 2.5 g (c) and 4 g (d) $C_2H_{12}N_6O_4S$.

Detailed structural and morphological characteristics of the as-synthesized W-4 sample were observed by TEM. Fig. 4a clearly shows the formation of uniform nanowires with diameters of 30–60 nm. The magnified TEM image of a single nanowire and its corresponding SAED pattern are shown in Fig. 4b–d, respectively. A typical h-WO_3 nanowire with a diameter of 50 nm that lay flat on the copper grid is shown in Fig. 4b. Clear lattice fringes (inset Fig. 4b) that correspond to the (001) crystalline plane of h-WO_3 with a d-spacing of 0.372 nm are present. These indicate the single-crystal quality of the WO_3 nanowire. Combined with the SAED pattern (Fig. 4d) of this individual nanowire we found that the as-prepared WO_3 product consists of single-crystalline nanowires with a preferred orientation along the [001] direction, and this is in accordance with the XRD result.

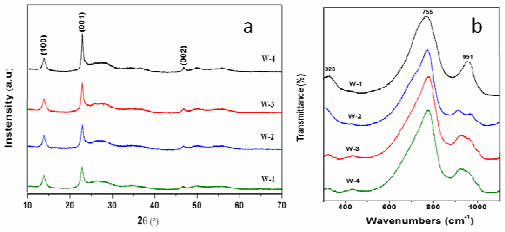

Fig.3. XRD patterns (a) and Raman spectra (b) of the WO_3 samples prepared via hydrothermal treatment at 170 °C for 24 h with addition of different amounts of $C_2H_{12}N_6O_4S$

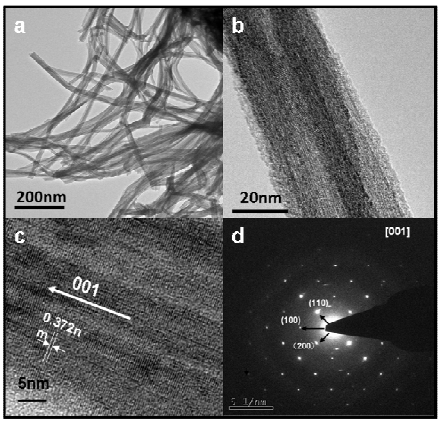

Fig.4 TEM image (a), HRTEM images (b, c) and SAED pattern (d) of W-4 sample.

Based on the investigations described above and the experiment results, we believe that $C_2H_{12}N_6O_4S$ acts as a stabilizer to facilitate the generation of the metastable hexagonal phase and it also functions as a structure directing agent to assist in the construction of nanowires. The structure of hexagonal phase WO_3 consists of WO_6 octahedra arranged as six-membered rings by sharing the equatorial oxygen in the *a*–*b* plane, resulting in the formation of trigonal cavities and hexagonal windows .[23,33] In the *c*-axis, WO_6 octahedra form 4-coordinated square windows. These lattice voids are capable of accommodating cations of appropriate size and the introduced cations can stabilize the metastable hexagonal crystal. In this study the formation of h-WO_3 nanowires occurred as follows:[25]

$$2HCl + Na_2WO_4 + nH_2O \leftrightarrow H_2WO_4 \cdot nH_2O + 2NaCl \quad (3)$$

$$H_2WO_4 \cdot nH_2O \leftrightarrow h\text{-}WO_3 + (n+1)H_2O \quad (4)$$

Tungstic acid is synthesized from sodium tungstate dehydrate in acidic solution at room temperature.[25,34] A hydrothermal process in the presence of $C_2H_{12}N_6O_4S$ results in the rapid formation of WO_3 nuclei from the precursors. Many researchers have reported that SO_4^{2-} ions play many important roles in the formation of 1D h-WO_3 nanowires.[28,29] SO_4^{2-} ions preferentially adsorb onto the faces parallel to the *c*-axis of the WO_3 nanocrystal and thus 1D nanowires are formed. Experiments have also indicated that the formation of h-WO_3 nanowires depends on the initial reagent $C_2H_{12}N_6O_4S$. The effect of other inorganic salts such as $C_2H_5N_3 \cdot HCl$, $C_2H_{10}N_6 \cdot H_2CO_3$ and $C_2H_{10}N_4S$ instead of $C_2H_{12}N_6O_4S$ were investigated with the conditions of the reaction system being the same. No WO_3 nanowires were obtained and the crystallization behavior changed significantly (Fig.S2 and S3).

Therefore, SO_4^{2-} ions play a critical role in the shape control processes. Additionally, during nuclei formation negatively charged tungsten species adsorb positively charged ions such as Na^+ and NH_4^+.[21] These ions can penetrate the frame of h-WO_3 and stabilize the metastable hexagonal crystal. A more concentrated positive ion solution will thus stabilize the solid state nuclei.[35-36] To study the effect of cation of salts on the crystal-phase of the products, Na_2SO_4, Li_2SO_4 NH_4Cl and $(NH_4)_2SO_4$ were selected. The results shows (Fig.S4) the pure phase of h-WO_3 was obtained when one of ammonium salts was added, Li+ and Na^+ did not produce the h-WO_3. Thus, it is suggesting that ammonium ions are believed to play a crucial role as stabilizing ions in the hexagonal and triangular tunnels during the formation of h-WO_3. [25 , 37-39]

N_2 adsorption–desorption isotherms of the WO_3 that was prepared with the addition of $C_2H_{12}N_6O_4S$ were obtained by the BET method for specific surface area calculations. As shown in Fig.5, Type III isotherms with a hysteresis loop indicative of small slit-shaped pores in the samples are evident. The BET surface area of the WO_3 samples were 25.70, 47.32, 77.93 and 148.31 m^2 g^{-1} for $C_2H_{12}N_6O_4S$ additions of 0, 1.5, 2.5 and 4 g, respectively. This suggests that the specific surface area of h-WO_3 increased significantly upon the addition of $C_2H_{12}N_6O_4S$ in the hydrothermal process. Conversely, the surface area of the WO_3 prepared with the addition of 5 g $C_2H_{12}N_6O_4S$ decreased to 64.72 m^2 g^{-1} because of the stacked nanowires (Fig. S1). These results are consistent with the SEM results. A comparison of the surface area of the h-WO_3 nanomaterials with various capping agents is shown in Table 1. The prepared h-WO_3 that was obtained in this study has a relatively high surface area and can thus potentially be used for the removal of Sr from waste solutions.

Table1 Comparison of the surface area of the prepared h-WO_3 nanomaterials with those prepared using hydrothermal route

Capping agents	BET surface area (cm^2 g^{-1})	Reference
$NaHSO_4$	27.83	24
Na_2SO_4	34.6	23
Na_2SO_4	42.62	40
$(NH_4)_2SO_4$	98	39
$(NH_4)_2SO_4$	104	25
$C_2H_{12}N_6O_4S$	148.31	In this work

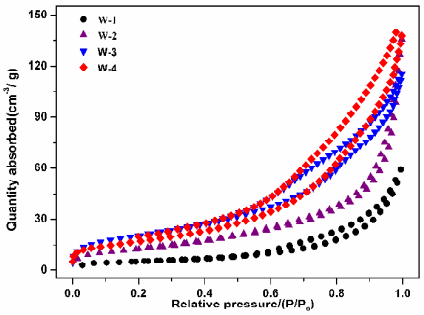

Fig.5 N_2 adsorption-desorption isotherms curves of WO_3 samples prepared via hydrothermal

FT-IR spectra of the WO_3 samples are shown in Fig. 6. The FT-IR spectra are almost the same for all the samples prepared with different amounts of $C_2H_{12}N_6O_4S$. The broad peak observed at 3141 cm^{-1} is attributed to the stretching vibration of surface hydroxyls and adsorbed water molecules.[41] The peaks at 1623 cm^{-1} is related to the bending vibrations of adsorbed water molecules.[42] **This indicates that the –OH might be bonded to W atoms.** The peaks at 1400cm^{-1} corresponds to the N-H vibration.[43] The strong peaks at 723 cm^{-1} can be attributed to the stretching vibration of W-O_{inter}-**W**, and the relatively weak intensity peaks at 657 cm^{-1} and 588 cm^{-1} can be assigned to the bending vibration of W-O.[44] Furthermore, we found that the intensity of the peak at 1400 cm^{-1} increased with an increase in $C_2H_{12}N_6O_4S$ content. This indicates that high amounts of hydroxyl groups and adsorbed water are present on the surface of the WO_3 sample after the addition of **$C_2H_{12}N_6O_4S$**, which is beneficial for the adsorption of Sr^{2+}.

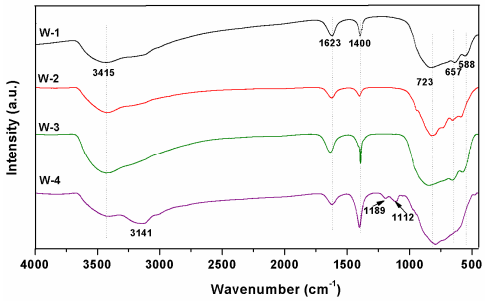

Fig.6. FT-IR spectra of WO_3 samples prepared via hydrothermal treatment at 170 ^{0}C for 24 h upon the addition of different amounts of $C_2H_{12}N_6O_4S$

3.2 absorption experiment

3.2.1 Effect of $C_2H_{12}N_6O_4S$ content

Fig. 7 shows the influence of different amounts of $C_2H_{12}N_6O_4S$ on the Sr^{2+} adsorption capacity of the WO_3 samples. Increases in Sr^{2+} adsorption with an increase in the amount of $C_2H_{12}N_6O_4S$ were initially observed followed by a decrease in Sr^{2+} adsorption with a further increase in $C_2H_{12}N_6O_4S$ content. Maximum Sr^{2+} adsorption occurred at an optimum $C_2H_{12}N_6O_4S$ content of 4 g. The reduction in Sr^{2+} adsorption at the higher $C_2H_{12}N_6O_4S$ concentration may be explained by the stacked nanowire morphology of the samples upon the progressive addition of $C_2H_{12}N_6O_4S$ (Fig.S1). Adding excessive amounts of $C_2H_{12}N_6O_4S$ can lead to a decrease in the surface area of the WO_3 sample and this reduces the number of active adsorption sites and the adsorption capacity. The WO_3 sample prepared with the addition of 4 g $C_2H_{12}N_6O_4S$ was used as the optimal sorbent in subsequent experiments.

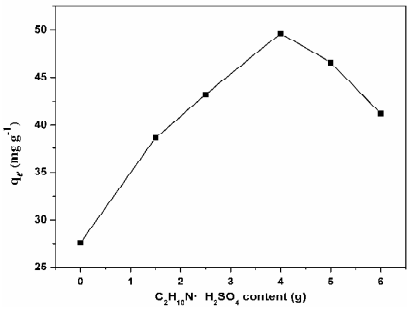

Fig.7. Effect of $C_2H_{12}N_6O_4S$ content on the Sr^{2+} adsorption by WO_3

samples (experiment conditions: 180 mg L^{-1} Sr^{2+}, adsorbent dose 3g L^{-1}, temperature 15°C)

3.2.2 Effect of initial pH

The pH of the medium had a significant influence on Sr^{2+} adsorption behavior because it changed the adsorbent's surface charge. The effect of pH on Sr^{2+} adsorption is shown in Fig.8. The uptake of Sr^{2+} by the W-4 sample is much greater than that of the W-1 sample at all pH values. The Sr^{2+} adsorption capacity of the W-1 sample increased slowly over the whole pH range. The sorption curve of W-4 increased sharply when the solution pH was increased to higher than 2 and the optimal Sr^{2+} adsorption capacity had a pH range of 6.0-7.0. Therefore, Sr^{2+} adsorption onto the W-4 sample is strongly pH dependent. A decrease in the Sr^{2+} adsorption efficiency was observed at low pH values and this is in good agreement with previous reports. Sr^{2+} uptake under acidic pH conditions is suppressed because the excessive amount of protons competes with Sr^{2+} for available sorption sites. At higher pH most of the surface adsorption sites are deprotonated and, therefore, electrostatic interactions increase greatly. Additionally, decreased competition with hydronium ions leads to a higher Sr^{2+} adsorption capacity.

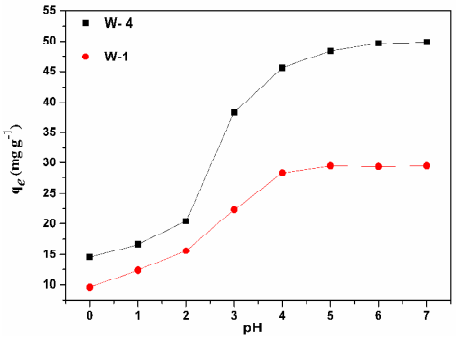

Fig.8. Effect of initial pH on the Sr^{2+} adsorption by WO_3 samples (experiment conditions: 180 mg L^{-1} Sr^{2+}, adsorbent dose 3g L^{-1}, temperature 15 °C)

3.2.3 Effect of contact time and adsorption kinetic

Sr^{2+} uptake as a function of contact time is shown in Fig. 9. Similar behavior was observed for WO_3. It is obvious that the Sr^{2+} adsorption equilibrium is reached fairly rapidly. A fast uptake of Sr^{2+} within 30 min was followed by slower uptake until the adsorption equilibrium was reached at around 90 min. Hence, a contact time of 2 h was adopted in subsequent experiments. The high initial uptake rate comes from the significant active site availability for Sr^{2+} sorption at the onset of the process. The distribution of wide pores on the adsorbents is also an important factor in the observed fast adsorption. The slow adsorption is associated with intraparticle diffusion of Sr^{2+} into the interior pores of the adsorbents.

Two kinetic models: a pseudo-first-order model[45] and a pseudo-second-order model[46] were used to describe the adsorption process. The pseudo-first-order kinetic model can be expressed in the following linearized form:

$$\log (q_e - q_t) = \log q_e - \frac{k_1}{2.303} t \qquad (5)$$

where t (min) is the contact time, k_1 (min^{-1}) is the pseudo-first-order rate constant, q_e (mg g^{-1}) and q_t (mg g^{-1}) represent the uptake of ions by the adsorbent at equilibrium and time t, respectively. k_1 and q_e can be calculated from the slope and the intercept of the plot of $\log(q_e - q_t)$ versus t.

$$\frac{t}{q_e} = \frac{1}{k_2 q_e^2} + \frac{t}{q_e} \qquad (6)$$

where k_2 (g mg^{-1} min^{-1}) is the pseudo-second-order rate constant. The values for k_2 and q_e can be calculated from the slope and the intercept of the plot of t/q_t.

The parameters of the two kinetic models were calculated and are listed in Table 2. The pseudo-second-order model provided better correlation coefficients (0.9912 and 0.9989) for W-1 and W-4, respectively. Therefore, the pseudo-second-order model is appropriate for a description of the kinetics for the whole adsorption process. This implies that chemical sorption may be the main rate limiting factor during the adsorption process.[47]

Table.2 kinetic parameters for Sr^{2+} sorption onto W-1 and W-4 (t=15 °C)

Model	Parameters	W-1	W-4
Experiment	q_e (mg g^{-1})	29.36	49.54
Pseudo first-order kinetic model	k_1 (min^{-1})	0.23	0.081
	q_e^{cal} (mg g^{-1})	28.95	49.17
	R^2	0.8756	0.9502
Pseudo second-order kinetic model	k_2 (g mg^{-1} min^{-1})	0.0028	0.0056
	q_e^{cal} (mg g^{-1})	29.32	49.32
	R^2	0.9912	0.9989

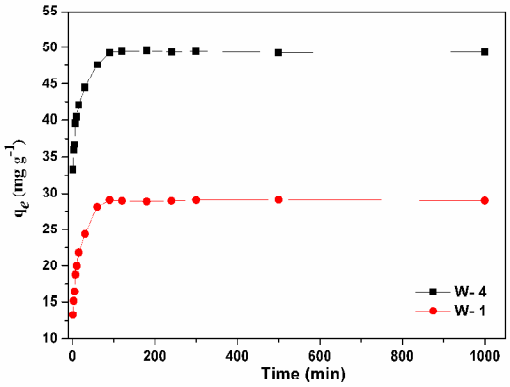

Fig.9. Effect of contact time on the Sr^{2+} adsorption by WO_3 samples (experiment conditions: 180 mg L^{-1} Sr^{2+}, adsorbent dose 3g L^{-1}, temperature 15 °C)

3.2.4 Effect of initial concentration and adsorption isotherms

Equilibrium adsorption studies were performed with samples of varying initial Sr^{2+} concentration from 20 to 200 mg L^{-1}. Fig. 10 shows that the adsorption capacity of the W-4 sample at equilibrium increased sharply as the initial Sr^{2+} concentration increased from 20 to 100 mg L^{-1} and it became nearly constant as the Sr^{2+} concentration was increased further. The adsorption isotherm profile is similar for the W-1 sample. At low Sr^{2+} concentrations of <100 mg L^{-1} the adsorption sites are unsaturated resulting in unsaturated Sr^{2+} adsorption. However, at higher Sr^{2+} concentrations (100-200 mg L^{-1}) the adsorption sites are insufficient for the adsorption reaction. The surfaces of the WO_3 particles can provide a copious amount of active adsorption sites and facilitate Sr^{2+} transport during the adsorption process. The different morphologies of W-4 and W-1 and their different specific surface areas (148.31and 25.70 m^2 g^{-1}, respectively)

contribute to the different amounts of active adsorption sites.

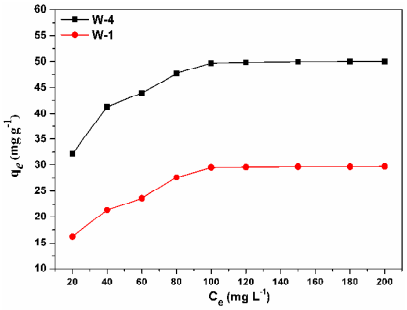

Fig.10. Effect of initial concentration on the Sr^{2+} adsorption by WO_3 samples (experiment conditions: 180 mg L^{-1} Sr^{2+}, adsorbent dose 3g L^{-1}, temperature 15 ^{0}C)

Langmuir[47] and Freundlich[48] isotherm models were used to describe the equilibrium data and they can be represented as follows:

Langmuir isotherm:

$$q_e = \frac{q_m b C_e}{1 + b C_e} \quad (7)$$

Freundlich isotherm:

$$q_e = k_f C_e^{\frac{1}{n}} \quad (8)$$

where C_e is the equilibrium concentration of the bulk solution (mg L^{-1}), q_e is the equilibrium concentration of the solid phase (mg L^{-1}), b (L mg^{-1}) is a constant related to the free energy or the net enthalpy of adsorption and q_m (mg g^{-1}) is the adsorption capacity at the isotherm temperature. k_f and n are equilibrium constants that are indicative of adsorption capacity and adsorption intensity, respectively.

The parameters calculated for the Langmuir and Freundlich isotherms are list in Table 3. As shown by the R^2 value the Freundlich model exhibits a good adsorption fit for Sr^{2+} by W-4 and W-1 compared to the Langmuir model. This suggests that the type of adsorption on W-4 and W-1 is multilayer adsorption. [45-46] The maximum absorption capacity (q_m) of the W-4 and W-1 samples is 52.93 mg g^{-1} and 29.87 mg g^{-1}, respectively, and this was calculated by fitting the Langmuir equation to the isotherm data. According to the measured BET surface area the as-prepared W-4 possesses a considerably higher specific surface area (148.31 m^2 g^{-1}) compared with the W-1 sample (25.70 m^2 g^{-1}). Therefore, the high surface area of W-4 is a factor that leads to its better water treatment performance. Table 4 shows a comparison of Sr^{2+} adsorption capacities for various adsorbents. It is apparent that the W-4 samples in this work have much higher adsorption capacities toward Sr^{2+} under acidic conditions and they may potentially be applied to radioactive solution treatment.

3.2.5 Effect of ionic strength

The adsorption experiments reveal that the extent of waste uptake is strongly influenced by the concentration and nature of the ionic electrolyte species that was added to the aqueous media. As shown in Fig. 11, the adsorption of Sr^{2+} onto the W-4 sample is strongly dependent on the cations present. The adsorption of Sr^{2+} is mainly controlled by strong cation exchange with cations such as Mg^{2+}, K^+ and Na^+. The competitive Sr^{2+} adsorption capacity decreases as follows: $Mg^{2+} \approx Li^+ > Na^+ > K^+$ at the same ionic concentration. This is attributed to the configuration of the hydrated metal ions in aqueous solution. The alkali metal ions are highly hydrated and smaller ions have a greater degree of hydration. The ionic radius increases in reverse order as follows: $Mg^{2+} \approx Li^+ > Na^+ > Sr^{2+} > K^+$. The hydrated Li^+, Mg^{2+} and Na^+ ions are thus larger than hydrated Sr^{2+}. It is thus more difficult to compete with hydrated Sr^{2+} for adsorption sites. K^+ ions have a smaller hydration radius than Sr^{2+} , and K^+ can compete more effectively with Sr^{2+} ions at the sorbent's surface.[52,53] Therefore, the size of the hydrated cations in the aqueous solution has an important effect on the Sr^{2+} adsorption process. Additionally, the Sr^{2+} adsorption capacity decreases with an increase in Na^+ concentration. Two factors may be responsible. First, high ionic strength creates a higher shielding effect toward Sr^{2+} adsorption onto the W-4 sample, which causes a decrease in adsorption. Second, competition between increasing amounts of Na^+ ions and Sr^{2+} ions for active sites on the W-4 sample might result in a decrease in adsorption.

Table 3 Equilibrium isotherm model parameters for Sr^{2+} adsorption on WO_3 sample

Model	Parameters	W-1	W-4
Langmuir isotherm	q_m (mg g^{-1})	29.87	52.93
	b (L mg^{-1})	0.0064	0.369
	R^2	0.923	0.875
Freundlich isotherm	k_f [mg g^{-1}(L/ g)$^{1/n}$]	10.11	15.4
	n	2.21	1.69
	R^2	0.9810	0.9956

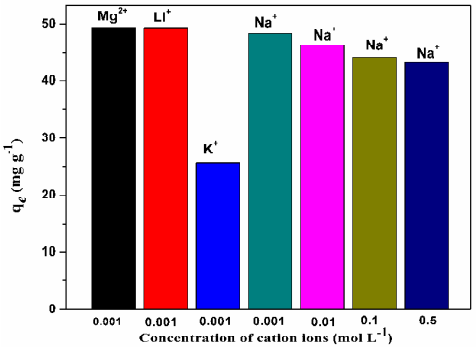

Fig.11. Effect of ionic strength on the adsorption of Sr^{2+} on W-4 sample.

3.2.6 Adsorption mechanism

To investigate the interaction mechanism between Sr^{2+} and the WO_3 samples the pH_{pzc} of the WO_3 samples were measured by plotting the zeta potential values of the particulate suspension solutions (3g L^{-1}) versus pH. As shown in Fig.12, the zeta potential values of the two samples are negative in the selected pH range. This indicates a highly negatively charged surface. Functional groups on the surface such as W=O and O–H are responsible for the surface negative charge and play an important role in the removal of metal ions. Moreover, the W-4 sample possesses more negative charges, which provides a favorable environment for the adsorption of positively charged Sr^{2+} through electrostatic interactions. This is illustrated by the surface of WO_3 containing more hydroxyl groups after the addition of $C_2H_{12}N_6O_4S$ leading to more negative charges.

Table 4 Comparison of the maximum adsorption capacities of Sr^{2+} on W-4 sample with other different adsorbents

Adsorbents	Solution condition	Adsorption capacity (mg g^{-1})	Reference
h-WO_3	pH=4.0	28.19	51
Ta-doped WO_3	pH=4.0	44.43	44
Hexagonal tungsten bronze (HTB)	1 M HNO_3	10.5	19
Mo-doped HTB	1M HNO_3	21.0	13
Nb-doped WO_3	**pH=4**	**54.39**	**15**
h-WO_3	pH=5	52.93	this work

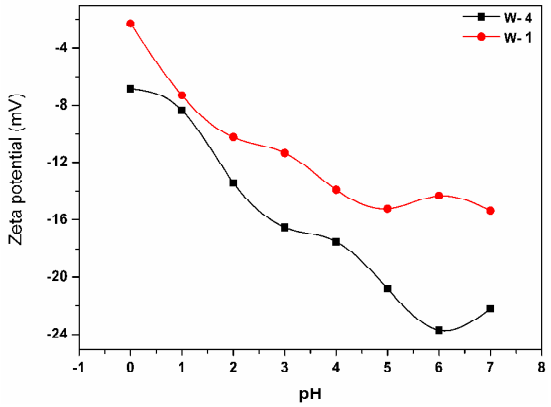

Fig.12. Zeta potential value as a function of pH for WO_3 samples prepared via hydrothermal treatment at 170 ^{0}C for 24 h with addition of different amounts of $C_2H_{12}N_6O_4S$

The difference in Sr^{2+} adsorption between W-1 and W-4 can be attributed to their distinct adsorption mechanisms. An electrostatic attraction between negative charges and positive charges mainly occurs on the surface of the adsorbents. Therefore, the BET surface area is an important factor in the electrostatic attraction process. The W-4 has a high surface area and exhibits far better adsorption performance toward Sr^{2+} than W-1. FT-IR, XPS and XRD were used to further investigate the interaction mechanism between Sr^{2+} and W-4. Fig. 13A shows FT-IR spectra of the samples before and after Sr^{2+} adsorption. The strong adsorption at 763 cm^{-1} comes from the ν(W–O–W) stretching vibration of the bridging and corner-sharing WO_6 octahedra in h-WO_3.[33] **The weak peaks at 1189 cm^{-1} and 1112 cm^{-1} come from the shortened W=O bonds of WO_3** and they degrade after Sr^{2+} adsorption. The peak at 1623 cm^{-1} corresponds to the δ(O–H–O) vibration of adsorption water.[43,44] After the adsorption of Sr^{2+} the new peaks at 736 cm^{-1}, 657 cm^{-1}, and 588 cm^{-1} come from ν(W–O) vibrations suggesting that the bridging O atoms play different roles within the WO_6 octahedra of h-WO_3.[42] The peaks at 3415 cm^{-1} and 1400 cm^{-1} are attributed to the stretching and bending vibrations of the –OH groups,[37] respectively, and they show a small decrease in intensity. Metal ions with empty orbitals are capable of accepting electron pairs while −OH groups with non-shared electron pairs can donate their electron pairs. The formation of −OH…Sr^{2+} is reasonable for the weakened bonding model of −OH groups. Therefore, electrostatic attraction occurs during Sr^{2+} uptake and we believe that an electrostatic attraction is responsible for Sr^{2+} adsorption on W-4. Nevertheless, the adsorption of Sr^{2+} onto h-WO_3 is attributed to both an electrostatic attraction and ion exchange. Ion exchange between Sr^{2+} and H^+, Na^+ occurs inside the tunnels of the h-WO_3 framework in addition to the surface. This was proven in the XPS and XRD discussion. As shown in Fig. 13B, a Sr^{2+} peak was observed in the Sr^{2+}-adsorbed W-4 and a doublet peak characteristic of Sr 3d appeared at 133.98 eV and 135.78 eV, respectively.[20] These can be assigned to Sr $3d_{5/2}$ and Sr $3d_{3/2}$, respectively. The peak at 133.98 eV is assigned to the Sr–OH bond suggesting the formation of a Sr compound. The O1s XPS spectra before and after the adsorption of Sr^{2+} are shown in Fig. 13C. The first strong peak at 529.8 e V corresponds to crystal lattice oxygen whereas the second shoulder peak at 531.4 e V corresponds to surface adsorbed oxygen.[52] After the adsorption of Sr^{2+} no peak was present at 531.4 eV indicating the formation of Sr–OH bonds. The XRD patterns of S1 before (a) and after (b) the adsorption of Sr^{2+} are shown in Fig. 13D. After the adsorption of Sr^{2+} the diffraction of the 001 peak shifted to lower angles. According to Bragg's law, a decrease in 2θ should result in an increase in lattice parameters. Thus the (001) plane spacing along the c-axis expanded when the larger Sr^{2+} exchanged with the H^+ or Na^+ that resided in the tunnels of h-WO_3.

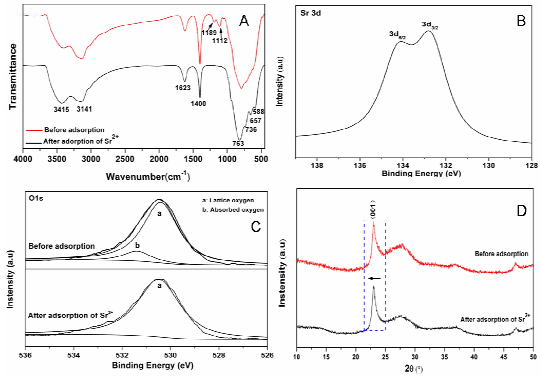

Fig. 13 (A) FT-IR spectra of W-4, (B) XPS spectra showing Sr 3d, (C) XPS spectra showing O1s, (D) XRD patterns of W-4.

Conclusions

In summary, h-WO_3 nanowires were successfully synthesized by a hydrothermal method with the assistance of $C_2H_{12}N_6O_4S$ The concentration of $C_2H_{12}N_6O_4S$ crucially influences the morphologies of the final product. The h-WO_3 samples have high BET surface areas and show excellent performance for the removal of Sr from an acidic aqueous solution. A maximum adsorption capacity of 52.93 mg g^{-1} was achieved in a pH range of 4.0–6.0. Adsorption kinetics is fast and adsorption is complete within 90 min. The Freundlich adsorption isotherm provided the best correlation for the equilibrium data of the W-4 sample. The presence of cations such as K^+ greatly inhibited the adsorption of Sr^{2+} whereas Na^+, Mg^{2+}, and Li^+ exhibited a mild effect on Cs^+ adsorption. The adsorption mechanism analysis results reveal that

the adsorption of Sr^{2+} on W-4 was regulated by ion exchange and surface complexation with hydroxyl groups. The latter plays a major role. From preliminary results we found that the W-4 sample exhibits great potential for the removal of Sr from radioactive waste solutions in engineering practice.

Acknowledgments

We wish to acknowledge the financial support from the Foundation of China Academy of Engineering Physics and the National Natural Science Foundation of China (no: 21471138)

Notes and reference

1 G. Tian, J. Geng, Y. Jin, C. Wang, S. Li, Z. Chen, H. Wang and Y. Zhao, J. Hazard. Mater., 2011, 190, 442–450.

2 Y. Zhao, C. Liu, M. Feng, Z. Chen, S. Li, G. Tian, L. Wang, J. Huang and S. Li, *J. Hazard. Mater*., 2010, 176, 119–124

3 A. Clearfield, *Solvent. Extr. Ion Exch*., 2000, 18, 655–678.

4 A. M. El-Kamash, *J. Hazard. Mater*., 2008, 151,432–445.

5 Y. Lan, Z. Su, X. Li, Z. Jiang, J. Xie and S. Li, *J. Radioanal. Nucl. Chem*., 2007, 273, 99–102.

6 K. Popa and C. C. Pavel, *Desalination*., 2012, 293, 78–86.

7 M. Manos and M. Kanatzidis, *J. Am. Chem. Soc*., 2012, 134, 16441–16446.

8 V. Luca C. S. Griffith, M. G. Blackford and J. V. Hanna, *J. Mater. Chem*., 2005, **15**, 564-572.

9 T. Mo¨ller, R. Harjula, M. Pillinger, A. Dyer, J. Newton, E.Tusa, S. Amin, M. Webb and A. Araya, *J. Mater. Chem.*, 2001, **11,**1526-1532.

10 L.H. Baetsle and D. Huys, *J. Inorg. Nucl. Chem.*, 1968, **30**, 639-674.

11 H. F. Pang, X. Xiang, Z. J. Li, Y. Q. Fu and X. T. Zu, Phys. Status Solidi A., 2012, 209,537-543.

12 A. Phuruangrat, D.J. Ham, S. J. Hong, S. Thongtema and J. S. Lee,J.Mater. Chem. 20 (2010) 1683

13 C.S. Griffith and V. Luca, Chem. Mater., 2004, 16, 4992-4999.

14 C.S. Griffith, V. Luca, J.V. Hanna, K. J. Pike, M. E. Smith and G. S. Thorogood, Inorg. Chem., 2009, 48,5648-5654.

15 B. J. Liu, W.J. Mu, X. Xie, X.L. Li, H.Y.Wei, Z.Y.Tan and S.Z. Luo, *RSC advances*., 2015,5,15603-15611.

16 T. Wen, X. L. Wu, M. C. Liu, Z.H. Xing, X. K. Wang and A. W. Xu, *Dalton Trans*., 2014,43,7464-7472.

17 J. M. Ortega, A. I. Martinez and C. R. *Magana, Sol. Energy, Mater.Sol .Cells*.,2006,90,2471-2478.

18 Y. Oaki and H. Imai, *Adv.Mate*r., 2006,18,1807-1813.

19 Z.Gu, H. Li,T. Zhai, W.Yang, G.Zhang and J.Yao, *J.Solid State Chem*., 2007, 180,98-95.

20 Y. Wu, Z. Xi, G. Zhang, J.Yu and D. Guo, *J.Cryst.Growth*., 2006, 292,143-149.

21 B. Liu and H. C. Zeng, *J. Am. Chem. Soc*., 2004, 126, 16744–16746.

22 Z. J. Gu, T. Y. Zhai, B. F. Gao, X. H. Sheng, Y. B. Wang, H. B. Fu, Y. Ma and J. N. Yao, *J. Phys. Chem. B*, 2006, 110,23829–23836.

23 W. Xiao, W. L. Liu, X. H. Mao, H. Zhu and D. H. Wang, *J. Mater.Chem*.,2013,1,1261-1269.

24 J. Li, X.H. Liu, Q.F. Han, X. X. Yao and X.Wang, *J.Mater.Chem*., 2013,1,1246-1253.

25 A.Phuruangrat, D. J. Ham, S. K. Hong, S. Thongtem and J. S. Lee, *J.Mater.Chem*., 2010,20,1683-1690.

26 Z. Czapla, J. Komar, T. Marciniszyn and R. Poprawski, *Solid State Ionics*., 2011,196,25-29.

27 M.J. Bushiri, C.J. Antony and M. Fleck, *J. Raman Spectrosc*., 2008, 39, 368-374.

28 I. M. Szilágyi, J. Madarász, G. Pokol, P. Király, G. Tárkányi, S. Saukko, J. Mizsei, A. L. Tóth, A. Szabó and K. Varga-Josepovits, *Chem. Mater.*, 2008, 20, 4116-4122.

29 C. Santato, M. Odziemkowski, M. Ulmann and J. Augustynski, *J. Am. Chem. Soc*., 2001, 123, 10639–10649.

30 J. H. Ha, P. Muralidharan and D. K. Kim, *J. Alloys Compd*., 2009,475,466-472.

31 M. F. Daniel, B. Desbat, J. C. Lassegues, B. Gerand and M. Figlarz, *J. Solid State Chem*., 1987, 67, 235-239.

32 G. L. Frey, A. Rothschild, J. Sloan, R. Rosentsveig, R. Popovitz-Biro and R. Tenne, *J. Solid State Chem*., 2001, 162, 300-306.

33 S. Balaji, Y. Djaoued, A. S. Albert, R. Z. Ferguson and R. Bruning, *Chem. Mater*., 2009, 21, 1381–1389.

34 X.C.Song, Y. F. Zheng, E. Yang and Y. Wang, *Mater.lette*., 2007, 61, 3904-3909.

35 I. M. Szilágyi, I. Sajó, P. Király, G.Tárkányi, A. L. Tóth, A. Szegedi, Katalin Varga-Josepovits and G. Pokol, *J Therm Anal Calorim.*, 2009, 98, 707-716.

36 I. M. Szilágyi, B. Fórizs, O. Rosseler, A. Szegedi, P. Németh, P. Király, G.Tárkányi, B. Vajna, Katalin Varga-Josepovits, K. László, A. L. Tóth, P.Baranyai and M.Leskel, *J Catal* 2012, 294, 119-127.

37 K. Huang, Q. Pan, F. Yang, S. Ni, X. Wei and D. He, *J. Phys. D: Appl. Phys*., 2008, 41, 155417.

38 Z. Gu, H. Li, T. Zhai, W. Yang, Y. Xia, Y. Ma and J. Yao, *J. Solid State Chem.*, 2007, 180, 98.

39 J. Zhang, J.P. Tu, X. H. Xia, X. L.Wang and C.D. Gu, *J. Mater.Chem*., 2011,21,5492-5498.

40 J. C. Shi, G.J. Hu, R. Cong, H. J.Bu and N. Dai, *New J. Chem*.,2013,37,1538-1544.

41 Z. Y. Liu, D. D. Sun, P. Guo and J. O. Leckie, *Chem. – Eur. J*., 2007, 13, 1851–1855.

42 A. Rougier, F. Portemer, A. Quédé, A.E. Marssi, *Appl. Surf. Sci*.,1999, 153, 1-7.

43 D.Hunyadi,I.Sajó, I. M. Szilágyi, *J Therm Anal Calorim*.,2014,116, 329-337.

44 X. L. Li, W. J. Mu, X. Xie, B. J, Liu, H.Tang, G. H. Zhou, H. Y. Wei, Y. Jian and S. Z. Luo, *J. Hazard. Mater*., 2014, 264, 386–394.

45 G. N. Manju, C. Raji and T.S. Anirudhan, Water Res., 1198, 32, 3062–3070.

46 Y. S. Ho, and G. McKay, Process.Biochem., 1999, 34, 451–465.

47 H. Para, M. Sudersanan, Water Res., 2010, 44, 854–860.

48 I. Langmuir, J. Am. Chem. Soc.,1918, 40, 1361–1403.

49 K.R. Hall, L.C. Eagleton, A. Acrivos and T. Vermeulen, Ind. Eng. Chem.Fundam., 1966, 5, 212–223.

50 S. B. Yang, C. Han, X. K.Wang and M.Nagatus, *J. Hazard. Mater*., 2014,274, 46-56

51 X. L. Li, W. J. Mu, X. Xie, B. J, Liu, W. B. Zhong, H. Y. Wei,Y. Jian, S. Z. Luo and L. S.Jian, J Radioanal Nucl Chem., 2013, 298:47–53

52 T. Wang, W. Liu, L. Xiong, N. Xu and J. R. Ni, *Chem. Eng. J*.,2013, 215-216, 366–374.

53 I. M. Szilágyi1, J. Madarász, G. Pokol, F. Hange, G. Szalontai,Katalin Varga-Josepovits and A. L. Tóth, J Therm Anal Calorim., 2009,97,11-18.

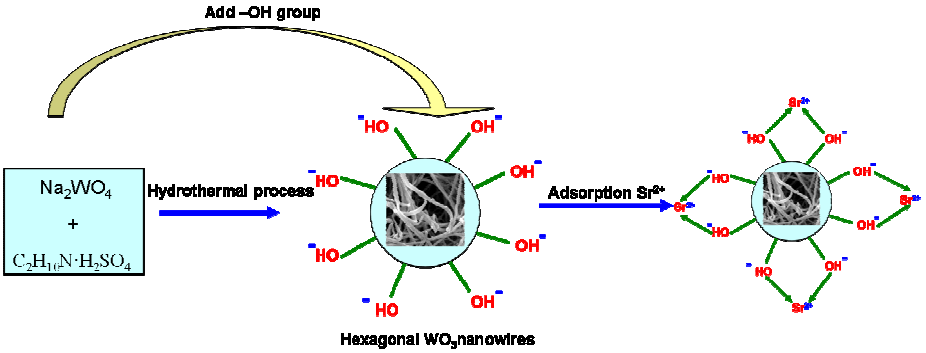

The prepared hexagonal WO_3 nanowires with the assistance of $C_2H_{10}N{\cdot}H_2SO_4$ possesses a large specific surface area and numerous adsorption functional groups, consequently improving the Sr^{2+} adsorption capacity considerably.